16 Physical Systems Biology and non-equilibrium Soft Matter

C.M. Aegerter, D. Assmann, G. Ghielmetti, U. Nienhaus, M. Schindlberger (Master Student) till 10.11, and T. Schluck

in collaboration with: Institute of Molecular Life Sciences (K. Basler, T. Aegerter-Wilmsen, C. Lehner, S. Luschnig), ETH Zürich (E. Hafen, I. Sbalzarini, P. Koumoutsakos), EPF Lausanne (P. Renaud, D. Floreano), University of Lausanne (S. Bergmann), Biozentrum Basel (M. Affolter), University of Strasbourg (N. Rivier), University of Fribourg (A. Jazwinska), University of Konstanz (G. Maret, W. Bührer, T. Sperling, N. Isert), New York University (C.C. Maass), Deutsches Luft- und Raumfahrtzentrum (M. Sperl), University of Twente (A. Mosk), Universite Joseph Fourier Grenoble (S. Skipetrov, F. Graner), Technion Haifa (E. Akkermans).

Work in the group of physical systems biology and non-equilibrium soft-matter is concerned with the study of developmental biology using physical techniques and study of light transport in turbid media. This is both in light of fundamental processes as well as applications for imaging in turbid media in particular biological systems. Moreover, the group works on the study of inherent non-equilibrium systems that can be tracked physically, such as driven granular gases. In the last year, we have made considerable progress in several of these areas, two of which are discussed in detail below. These subjects concern the transport of light in turbid media and the transition to Anderson localisation of light and the development of a method for three dimensional microscopy behind extremely turbid layers.

16.1 Localization of light

The quest for the experimental demonstration of Anderson localisation [1] in a three dimensional disordered medium has a very long history [2–7] and clear-cut evidence for that transition has only been shown very recently by our group using time-resolved transmission experiments [8, 9]. The main hindering property of extremely turbid samples is that absorption is always dominating the transport through thick and turbid samples [6, 7]. This can be resolved with time dependent measurements since localisation and absorption have different signatures in the time dependent transmission through a sample. However, a direct study of the mean square spread of the photon cloud $\langle r^2 \rangle = \sigma^2$ transported though a sample presents a much clearer measure for the transport properties of a sample [10]. For instance, because all photons measured in this way have spent the same amount of time inside the sample, meaning that they are all equally affected by absorption. Thus a determination of the mean square width of the transmitted light is completely independent of absorption and presents a direct measure of the transport mechanism. For turbid samples (all samples discussed here are TiO_2 nanoparticles with diameters in the range of 200 nm), this transport is diffusive, which means that the width σ^2 increases linearly with time for all times [10]. This can be seen in Fig. 16.1, where the time dependence of σ^2 is shown for a diffusive sample with a turbidity of $kl^* = 6.8$. Note that for these samples the absorption length as determined from static transmission measurements is shorter than the sample thickness, but the measured width can exceed the thickness.

The width of the photon distribution is determined using a pulsed laser system and an ultra-fast gated CCD camera. The incoming pulsed laser (pulse duration 100 fs) is focused on the surface of the sample and the transmitted light is imaged onto the CCD camera. the camera is coupled to an image intensifier, with a gate that can be opened on a very short time scale (1 ns). This opening can be scanned with a time resolution of 250 ps. Due to the repetition rate of the laser of 80 MHz, many different laser pulses impinge onto the sample dur-

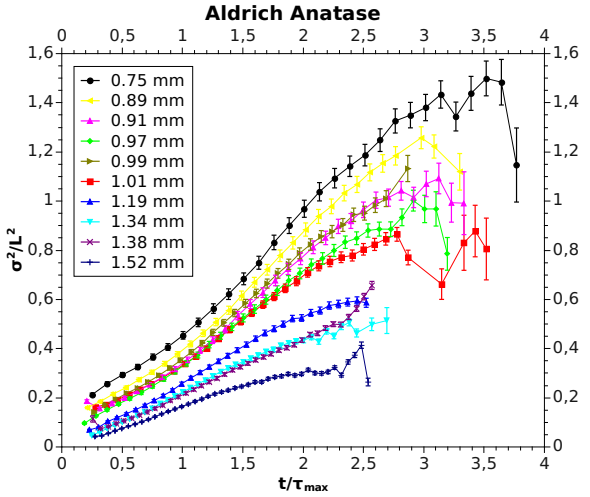

FIG. 16.1 – *The mean square width scaled with the sample size* $\frac{\sigma^2}{L^2}$ *for a diffusive sample with a scattering strength of* $kl^* = 6.8$. *The time axis is scaled with the diffusion time* $\tau_{max} \propto L^2/D$. *The width increases linearly over the whole time window, also exceeding the thickness of the sample. This shows that absorption does not play a role in the determination of the width. The slope of the curve corresponds directly to the diffusion coefficient of light in the sample.*

ing a measurement of the CCD with a given setting of the opening, such that an image of very fast processes can be taken. Thus we obtain snapshots of the light distribution behind the samples at different times.

This is shown in Fig. 16.2, where also the contours of a Gaussian fit determining the width is shown. In the sample shown, the width increases at early times, but then stays constant. This behaviour is expected for extremely turbid samples, where localisation of light sets in, corresponding to a limiting length scale of the localisation length [10].

This is shown in more detail in the time and thickness dependence of the width of an even more turbid sample (R700) shown in Fig. 16.3. Here again the width as determined from the intensity measurements as described before are shown. Initially, the width increases linearly as expected for a diffusive process. However at later times, the width saturates and remains constant for thick samples. Such behaviour of light in a random medium means

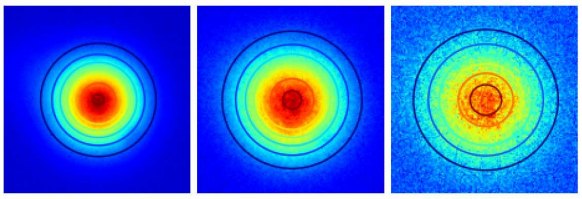

FIG. 16.2 – *A section of the raw data (with the fit displayed via contours) of a R104 sample that features a plateau. From left to right the timestamps are 4, 6 and 8 ns after the initial laserpulse. From 4 to 6 ns one can see a broadening in the profile width, whereas from 6 to 8 ns no further increase can be seen. This constant profile width is the signature of Anderson localisation.*

that the transport of light by diffusion has been limited to the corresponding length scale. This localisation length can only be observed for extremely turbid samples with $kl^* \simeq 1$ [11], in three dimensional media [12]. In this case, light traveling on closed loops interferes with itself, leading to a breakdown of transport on scales bigger than

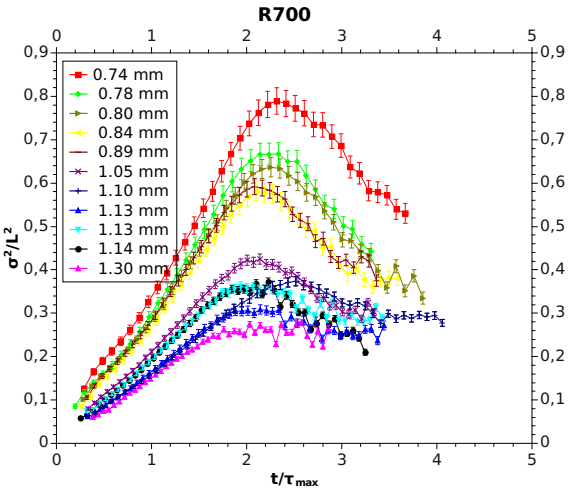

FIG. 16.3 – *The mean square width scaled with the sample size* $\frac{\sigma^2}{L^2}$ *for the sample with the highest turbidity* $kl^* = 2.7$, *R700. For this sample, the spread of the photon cloud comes to a halt at a length scale corresponding to the localisation length. This plateau can be clearly seen in the samples with the biggest thickness. When the sample thickness becomes comparable to the localization length, additional effects come into play which lead to an effective reduction of the width as a function of time.*

these loops. In Fig. 16.3, one can also observe that for thinner samples, the width can even decrease with time, which is not expected. This can, however, be understood in a statistical picture of localisation, where a range of localisation lengths corresponding to differently sizes loops exist. For thin samples, only the smaller loops can be populated at long times leading to a decrease of the average width.

The samples shown in Fig. 16.3 all had the same turbidity and thus the same localisation length. However, as the critical turbidity for the transition to localisation is approached, the localisation length diverges and localisation can no longer be observed when the localisation length becomes comparable to the sample thickness [12, 13]. A way of studying the turbidity dependence of the localisation length is via a change in the wavelength of the incoming light in one and the same sample. Due to a change in scattering cross-section with wavelength, different turbidities are obtained for different wavelengths. The turbidities are determined using coherent backscattering [14, 15]. Such a dependence of the width with incoming wavelength is shown in Fig. 16.4 for a sample as in Fig. 16.3 with a thickness of $L = 0.98mm$. As the wavelength increases, so does kl^* and we move gradually to the transition to diffusive behaviour. At the highest value of $kl^* = 3.5$, the width does no longer saturate completely, but rather shows a sub-diffusive increase.

This can be observed more clearly in the case of a sample with higher kl^*, ranging from $kl^* = 5$ to 6, as shown in Fig, 16.5. Here at the highest value of kl^*, a linear increase is observed indicating diffusive behaviour, but at lower values of kl^* a slower increase in σ^2 is seen. This corresponds to the mobility edge of the transition, where the transport can still take place however is slowed down due to interference effects. Theory predicts a re-scaling of the diffusivity inversely proportional to the thickness, which is in good agreement with the observed time dependence of the increase of σ^2 [16, 17]. This behaviour has already been observed studying the time dependence of the with of ultra-sound transported through turbid media [18].

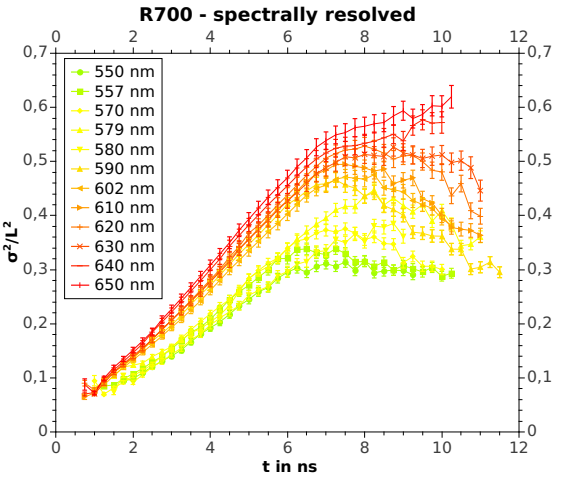

FIG. 16.4 – *Spectral measurement of a R700 sample in the range 550 – 650 nm. At larger wavelength the turbidity kl^* increases and localising effects get stronger as can be seen via the lower mean square width σ^2_∞ of the plateaus. For wavelengths above 650 nm one observes starting of a breakdown of localisation to a sub-diffusive behaviour.*

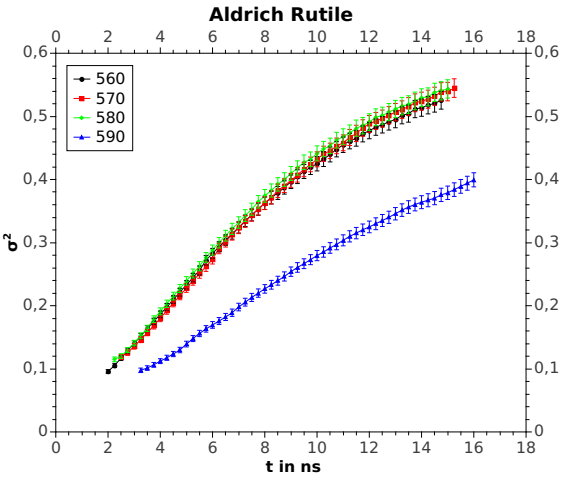

FIG. 16.5 – *The spectral measurement of a sample which is diffusive at a wavelength of 590 nm. With decreasing wavelength λ the turbidity kl^* increases, leading to the establishment of sub-diffusive behaviour. However, the width keeps increasing with time indicating that strong localization of light has not yet been reached for the corresponding turbidities down to $kl^* = 5.4$. However, these data clearly indicate the presence of the mobility edge, where the diffusion coefficient scales inversely with the sample thickness.*

[1] P.W. Anderson, Phys. Rev. **109**, 5 (1958).

[2] Y. Kuga and A. Ishimaru, J. Opt. Soc. Am. A **1**, 831 (1984).

[3] M.P. van Albada, and A. Lagendijk, Phys. Rev. Lett. **55**, 2696 (1985).

[4] P.E. Wolf, and G. Maret, Phys. Rev. Lett. **55**, 2696 (1985).

[5] J.M. Drake and A.Z. Genack, Phys. Rev. Lett. **63**, 259 (1989).

[6] D.S. Wiersma, P. Bartolini, A. Lagendijk, *et al.*, Nature **390**, 671 (1997).

[7] F. Scheffold, R. Lenke, R. Tweer, *et al.*, Nature **398**, 206 (1999).

[8] M. Störzer, P. Gross, C.M. Aegerter and G. Maret, Phys. Rev. Lett. **96**, 063904 (2006).

[9] C.M. Aegerter M. Störzer, and G. Maret, Europhys. Lett. **75**, 562 (2006).

[10] N. Cherroret, S.E. Skipetrov and B.A. van Tiggelen, Phys. Rev. E **82**, 056603 (2010).

[11] A.F. Ioffe and A.R. Regel, Progress in Semiconductors **4**, 237 (1960).

[12] E. Abrahams *et al.*, Phys. Rev. Lett. **42**, 673 (1979).

[13] R. Berkovits and M. Kaveh, J. Phys. C: Cond. Mat. **2**, 307 (1990).

[14] P. Gross, M. Störzer, S. Fiebig, M. Clausen, G. Maret, and C. M. Aegerter, Rev. Sci. Instrum. **78**, 033105 (2007).

[15] S. Fiebig, C.M. Aegerter, W. Bührer, M. Störzer, E. Akkermans, G. Montambuax and G. Maret, EPL **81**, 64004 (2008).

[16] D. Vollhardt and P. Wölfle, Phys. Rev. B **22**, 4666(1980).

[17] S.E. Skipetrov and B.A. van Tiggelen, Phys. Rev. Lett. **96**, 043902 (2006).

[18] H. Hu, A. Strybulevych, J.H. Page, S.E. Skipetrov and B.A. van Tiggelen, Nature Phys.**4**, 945 (2008).

16.2 Three dimensional microscopy in turbid media

Apart from studies into the fundamental aspects of light transport in turbid media, we are also applying our know-how in this field to create applications in the realm of imaging in turbid media. The main difficulty to image structures in living systems lies in the fact that many tissues are turbid, such that no focus can be formed and thus no image plane can be detected.

Using wave-front shaping, we have invented a technique to overcome this and be able to obtain scanning fluorescence images at optical resolution behind turbid layers that are completely intransparent [1]. This was already described in a previous annual report and rests on principles of wave-front shaping to create a focus [2] and the memory effect [3–5]. The same principle has been used subsequently to obtain optical resolution images behind turbid layers where the focus is created via phase conjugation of the outgoing light [6]. We have now expanded the technique to be able to obtain three dimensional fluorescence images behind similarly turbid screens [7]. To understand the principles of this we quickly review the basics of the memory effect and how this is used to scan a focus.

The memory effect leads to a retention of correlation of the phase over an angular scale determined by the thickness of the turbid medium. This is because the light transport through the turbid medium is confined to a cone with a width corresponding to the thickness of the medium. This is for a point illumination. When considering different channels through the turbid medium as illuminated by different point sources, then a change of the incoming phase remains correlated within this cone. Thus, phase changes of the order of $qL \simeq 1$ remain conserved, where $q = \theta k$ is the overall scattering vector with $k = 2\pi/\lambda$ and L is the thickness of the layer [3–5]. In the application for a scanning microscope, the angle θ corresponds to the angle covering the field of view of the microscope. For the experiments presented here with a layer of thickness $L = 15\mu m$ and a wavelength of $\lambda = 488nm$, this angle is $\theta \simeq 5 \cdot 10^{-3}$.

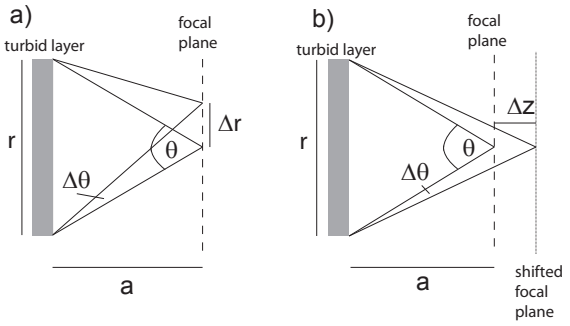

FIG. 16.6 – *Geometry of scanning in the different directions. The change in angle is limited by the memory effect. a) shows the situation for two-dimensional scanning in the $x-y$ plane. The change in angle here is given by $\Delta\theta = \Delta r/a$. In the z-direction in contrast, the change in angle is given by $\Delta\theta = r\Delta z/a^2$.*

For two-dimensional scanning in the $x-y$ plane, the angle determines directly the field of view together with the distance from the scattering layer a via $\Delta r = a\Delta\theta$. Thus, for a shift in the focal position, the phase of the incoming light must be changed by an amount corresponding to $\phi = kr \cdot \frac{\Delta r}{a}$. This change in phase is achieved by a tilting of the wave front by the galvo-scanner discussed above. In the geometry of our experiment, the intensity of the focus is halved over a distance of $\Delta r_{max} \simeq 5\mu m$, thus indicating the spatial resolution. For scanning in the z direction, the situation is slightly different, as illustrated in Fig. 16.6. The angle change now not only depends on the distance a, but also on the radial component. The shift in position is now given by $\Delta z = a^2\Delta\theta/r$, where the memory effect still correlates paths within the cone of angle $\theta \simeq 1/(kL)$. Again, this corresponds to a phase change of the incoming light of $\phi = kr^2 \cdot \frac{\Delta z}{a^2}$. This change in phase is obtained by adding a curvature to the incoming light field by adding a parabolic shift to the SLM, where the radius of curvature, R, corresponds to $1/R = \frac{\Delta z}{a^2}$.

Again, for the geometry of the experiment described here, this yields a scanning range of $\Delta z_{max} \simeq 60\mu m$. Thus, for this geometry, the field of view obtained in the z-direction can be increased with respect to that in the $x-y$ plane. This is true as long as the size of the illumination is smaller than the distance of the structure of interest from the scattering layer. However, this difference also leads to an anisotropy in the size of the focal spot. In the z-direction, the focal spot will be larger by a factor of a/r as compared to the $x-y$ direction. This is because of the difference in path lengths in the different directions causing the interference based focus. With the geometry described above, we expect a resolution in the $x-y$ plane given by half the wavelength of the light used, i.e. 250 nm and a resolution in the z-direction of $3\mu m$.

Fig. 16.7 shows a sequence of cuts through a fluorescent bead hidden behind a screen with a thickness of more than 10 mean free paths. Such a screen is completely intransparent and conventional imaging is impossible. Each cut shown in the figure is obtained by scanning the $x-y$ plane using a tilting of the incoming wave-front. The different cuts are made by adding a parabolic phase field to the SLM, leading to a shift of the focus in the z direction. The distance between successive cuts is $2\mu m$ for all images except between parts d,e and f, which are centered about the middle of the particle and are spaced by 1 μm. As can be seen from the different intensities of the article, the focus scans through the whole structure, but the resolution is worse than in the $x-y$ plane as discussed above. A determination of the width of the point-spread function in the z-direction gives a resolution of 3.0(1) μm in good agreement with the expectation. The scan range is illustrated in Fig. 16.8, where two fluorescent beads are positioned 55 μm apart, both within the plane of observation. The figure shows three cuts through the plane at different depths of 0, 30 and 55 μm. At a distance corresponding to the scan range in the z-direction, the quality of the focus deteriorates, such that the image quality is similarly worsened. However, as seen in Fig. 16.8c, we still observe the position of the second bead.

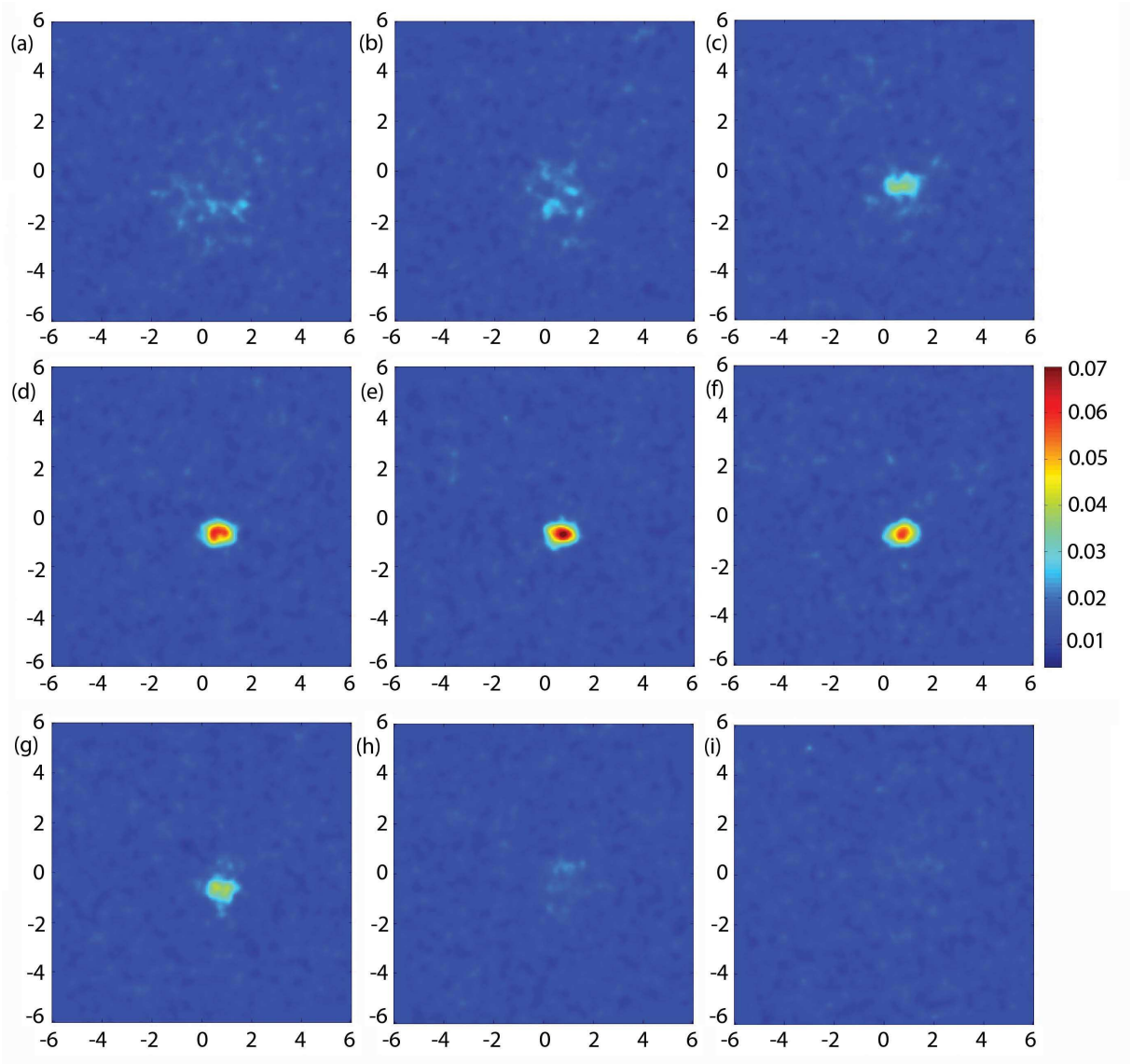

FIG. 16.7 – *The fluorescence signal of a single 450 nm diameter fluorescent bead hidden behind a turbid layer. The images show the scattered light fluorescence image of the same bead and on the same intensity scale, while the position of the focal plane differs between the images.*
In (a), the position is at -7 μm, behind the bead and consecutively moves forward in steps of 2μm, until it lies 7 μm in front of the bead position in image (i). The center of the bead, which would therefore lie between image (d) and its subsequent image has been added as well in part (e). Thus, the difference in z position between parts (d) and (e) as well as (e) and (f) corresponds to only 1 μm. The $x-y$ scan range in this case is 12x12 μm^2.

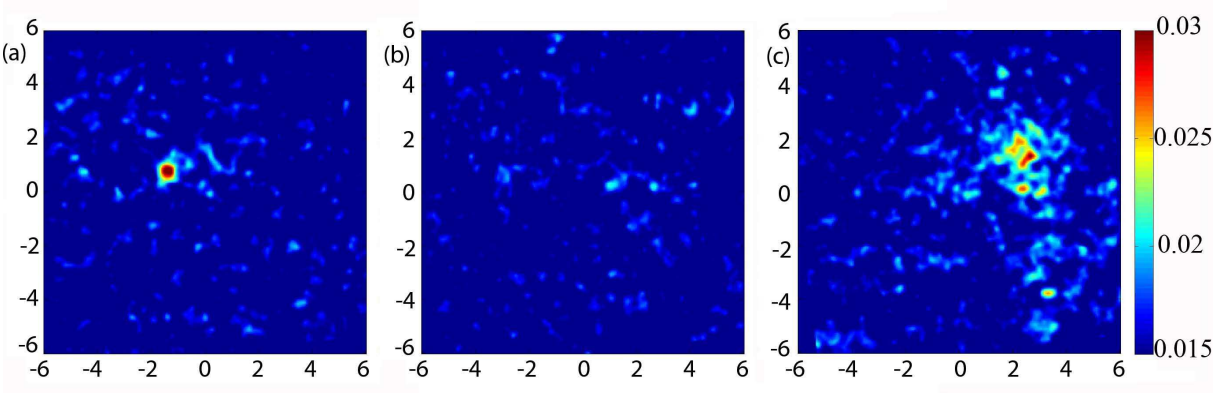

FIG. 16.8 – *The fluorescence signal of two 450 nm diameter fluorescent beads hidden behind an intrasparent turbid layer. The two beads are spaced 55 μm apart in the z-direction and are at positions (-2,-1) and (2,-2) respectively in the (x, y) plane. The images show the scattered light fluorescence image on the same intensity scale, at three different depth.*
In (a), the position is centered at the first bead, whereas at (b) the position is 30 μm towards the second particle. Figure (c) finally is at a z position of 55 μm corresponding to the position of the second particle. The scan range in this case is a window in the $x - y$ plane of 12x12 μm^2. As discussed in the text, the z scan-range is 60 μm explaining the deteriorating quality of the image of the second particle. However, the three dimensional structure of the beads' positioning can be clearly seen.

[1] I. M. Vellekoop and C.M. Aegerter,
Opt. Lett. **35**, 1245 (2010).

[2] I. M. Vellekoop and A. P. Mosk,
Opt. Lett. **32**, 2309 (2007).

[3] D.L. Fried, J. Opt. Soc. Am. 72, 52 (1982).

[4] S. Feng, C. Kane, P.A. Lee, and A.D. Stone,
Phys. Rev. Lett. **61**, 834 (1988).

[5] I. Freund, M. Rosenbluh, and S. Feng,
Phys. Rev. Lett. **61**, 2328 (1988).

[6] C. L. Hsieh, Y. Pu, R. Grange, G. Laporte,
and D. Psaltis,
Opt. Express **18**, 20723-20731 (2010).

[7] G. Ghielmetti and C.M. Aegerter,
Opt. Express **20**, 3744 (2012).